CMS Physics Analysis Summary

Contact: cms-pag-conveners-exotica@cern.ch 2019/07/10

Search for long-lived particles using delayed photons with proton-proton collisions at $\sqrt{s} = 13$ TeV

The CMS Collaboration

Abstract

A search for new physics with long-lived particles decaying to photons is presented using proton-proton collisions data at $\sqrt{s} = 13$ TeV collected by the CMS experiment in 2016 and 2017 corresponding to 35.9 fb^{-1} and 41.5 fb^{-1} of integrated luminosity, respectively. Results are interpreted in the context of supersymmetry with gauge-mediated supersymmetry breaking, where long-lived neutralinos are produced as secondaries and decay to a photon and a gravitino. Limits are presented as a function of the neutralino proper decay length and mass. For neutralino proper decay lengths of 10^1, 10^2, 10^3, and 10^4 cm, masses up to 320, 525, 360, and 215 GeV are excluded at 95% CL, respectively. We extend the previous best limits in the neutralino proper decay length by up to about one order of magnitude, and in neutralino mass by up to about 100 GeV.

1 Introduction

In this note, the results of a search for long-lived particles (LLP) decaying to a photon and a weakly-interacting particle are presented. The analysis uses the data set collected in 2016 and 2017 with the CMS detector at the CERN Large Hadron Collider (LHC), corresponding to integrated luminosities of 35.9 and 41.5 fb^{-1}, respectively. This search exploits the capability of the CMS electromagnetic calorimeter (ECAL) to measure photon arrival times with high precision in order to detect signatures of late-arriving photons produced at displaced vertices.

Neutral particles with long lifetimes are predicted in many models of physics beyond the standard model (SM). In this search, a benchmark scenario of supersymmetry (SUSY) [1–14], with gauge-mediated supersymmetry breaking (GMSB) [15–23] is presented, commonly referred to as the "Snowmass Points and Slopes 8" (SPS8) benchmark model [24]. In this scenario, pair-produced squarks and gluinos undergo cascade decays as shown in Figure 1, and eventually produce the lightest supersymmetric particle (LSP), the gravitino ($\widetilde{\text{G}}$), which is stable and weakly interacting. The phenomenology of such decays chains is primarily determined by the nature of the next-to-lightest supersymmetric particle (NLSP). In the SPS8 benchmark, the NLSP is the lightest neutralino, $\widetilde{\chi}_1^0$, where the mass of the NLSP is linearly related to the effective scale of SUSY breaking (Λ).

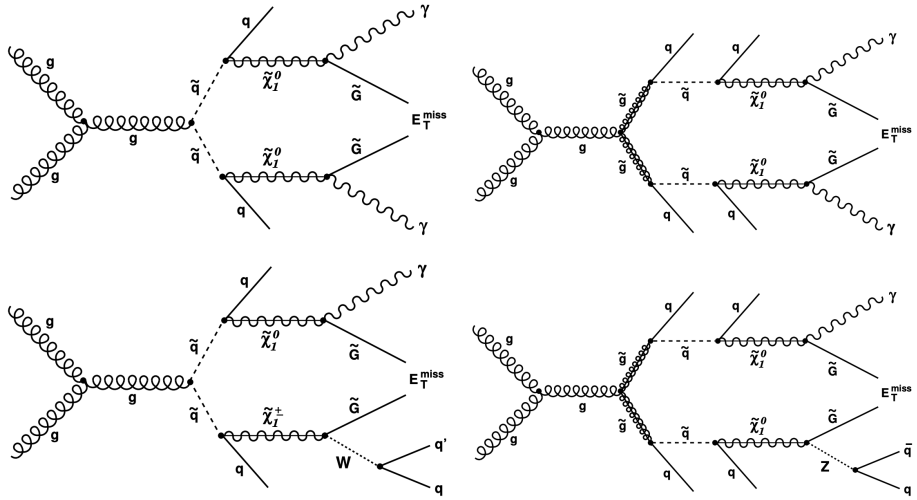

Figure 1: Example diagrams for SUSY processes that result in a diphoton (top) and single photon (bottom) final state through squark (left) and gluino (right) pair-production at the LHC.

Depending on the fundamental scale of SUSY breaking [15, 25], the coupling of the NLSP to the gravitino could be very weak and lead to long NLSP lifetimes. Λ is a free parameter in the SPS8 model set and determines the rate and primary mode of the production of supersymmetric particles. The dominant decay mode of the NLSP is to a photon and the gravitino, resulting in a final state with two photons, missing transverse momentum ($p_{\text{T}}^{\text{miss}}$), and potentially additional jets and other SM particles. If the NLSP has a proper decay length that is a significant fraction of the size of the CMS tracking volume, then the photons produced at a secondary vertex tend to exhibit peculiar features. They have significantly delayed arrival times at the ECAL (order of ns) and impact angles that point significantly away from the primary interaction vertex.

This search makes use of these features to identify such potential signals of physics beyond the SM. We select events with one or two photons consistent with a displaced or delayed signature, and three or more jets. Signal events are expected to produce significant amounts of $p_{\text{T}}^{\text{miss}}$ as the LSP escapes the detector volume without interacting with any active detector components.

In the case of very long-lived NLSPs, one of the NLSPs may completely escape the detector providing additional $p_{\mathrm{T}}^{\mathrm{miss}}$. Previously, similar searches for LLPs decaying to displaced or delayed photons have been performed by the CMS [26] and ATLAS [27] Collaborations using LHC collisions at a center of mass energy of 7 and 8 TeV, respectively.

2 The CMS detector

The central feature of the CMS apparatus is a superconducting solenoid of 6 m internal diameter, providing a magnetic field of 3.8 T. Within the solenoid volume are a silicon pixel and strip tracker, a lead tungstate crystal electromagnetic calorimeter (ECAL), and a brass and scintillator hadron calorimeter (HCAL), each composed of a barrel and two endcap sections. The ECAL is highly granular and consists of 61200 crystals in the barrel region, each with an area of approximately 2.2×2.2 cm^2 corresponding to roughly 0.0174×0.0174 in η-ϕ space, where η is the pseudorapidity and ϕ the azimuthal angle of the coordinate system [28]. Each of the two endcap sections consist of 7324 crystals, each with an area of 2.68×2.68 cm^2. A typical electromagnetic shower spans approximately 10 crystals with energy deposits above noise threshold. The best possible time resolution for each ECAL channel is measured to be between 70 and 100 ps depending on the age of the detector. Forward calorimeters extend the pseudorapidity coverage provided by the barrel and endcap detectors. Muons are measured in gas-ionization detectors embedded in the steel flux-return yoke outside the solenoid. The first level of the CMS trigger system [29], composed of custom hardware processors, uses information from the calorimeters and muon detectors to select the most interesting events in a fixed time interval of less than 4 μs. The high-level trigger (HLT) processor farm further decreases the event rate from around 100 kHz to less than 1 kHz, before data storage. A more detailed description of the CMS detector, together with a definition of the coordinate system used and the relevant kinematic variables, can be found in Ref. [28].

3 Event samples

This analysis uses CMS data with total integrated luminosity of 77.4 fb^{-1} collected in pp collisions at $\sqrt{s}$ = 13 TeV in 2016 and 2017. Different triggers are used in 2016 and 2017, which will be discussed in detail in Section 4.1.

Simulated Monte Carlo event samples are used to model the SM backgrounds and signal contributions, primarily for the purpose of optimizing the event selection and the binning in the photon time and $p_{\mathrm{T}}^{\mathrm{miss}}$ observables.

The MADGRAPH5_aMC@NLO v2.2.2 generator [30] is used in next-to-leading order (NLO) mode to simulate events originating from single top quark and top quark pair production; and in leading-order (LO) mode to simulate events originating from QCD multijet, γ+jets and W+jets production. Simulated samples of diphoton events are generated using SHERPA v2.2.4 [31], and includes Born processes with up to three additional jets as well as box processes at LO accuracy. The SPS8 benchmark signal models are generated using PYTHIA v8.212 [32] to model the 2016 data set, and PYTHIA v8.230 to model the 2017 data set.

For all simulation samples discussed above, the fragmentation and parton showering is modeled using PYTHIA v8.212 with the CUETP8M1 tune [33] for the 2016 data set, and PYTHIA v8.230 is used with the CP5 [34] tune for the 2017 data set. The NNPDF3.0 [35] and NNPDF3.1 [36] parton distribution functions (PDFs) sets are used for the 2016 and 2017 simulation samples, respectively. The signal and background samples are simulated using a GEANT4-based model [37]

of the CMS detector, and model the effects of pileup, i.e. simultaneous multiple proton-proton collisions within a single bunch-crossing.

4 Trigger and event selection

The unique signature of delayed photons requires specialized triggers and photon reconstruction and identification criteria. The search selection is different for the 2016 and 2017 data sets, primarily due to the introduction of a targeted high-level trigger implemented for the 2017 data set.

4.1 Trigger selection

For the 2016 data set, events are selected by a diphoton trigger, requiring p_{T} larger than 42 and 25 GeV for the leading and sub-leading photons, respectively. Loose identification criteria are imposed on the ECAL shower width and the electromagnetic to hadronic energy ratio to reduce the rate of background from jets misidentified as photons.

For the 2017 data set, a dedicated high-level trigger was developed to select events with a single photon satisfying requirements consistent with production at a displaced secondary vertex. Such photons tend to impact the front face of the barrel ECAL at a nonnormal incidence angle, resulting in a more elliptical electromagnetic shower in the η-ϕ plane [26]. In addition to standard requirements on the shower width and electromagnetic to hadronic energy ratio, requirements on the major and minor axes are also imposed, which identifies this elliptical shower shape, described in more detail in Sec. 4.2. Loose requirements on the amount of energy around the direction of the photon in the CMS subdetectors (isolation) are also imposed on trigger photon candidates, and the p_{T} of the photon is required to be larger than 60 GeV. Electrons misidentied as photons are vetoed by requiring that the candidate photon be geometrically isolated from charged particle tracks. Relaxing the trigger requirement from two photons to only one photon increases the signal acceptance, particularly for signals with large lifetimes, but also significantly increases the rate of background. In order to suppress the background rate to a level acceptable for the operation of the HLT, the scalar sum of the p_{T} of all jets (H_{T}) is required to be larger than 350 GeV.

4.2 Object reconstruction and selection

Physics objects are defined using the particle-flow (PF) algorithm [38], which aims to reconstruct and identify each individual particle in an event using an optimized combination of information from the various elements of the CMS detector. The reconstructed vertex with the largest value of summed physics-object p_{T}^2 is selected as the primary interaction vertex.

Photon candidates are reconstructed from energy clusters in the ECAL [39] and identified based on the transverse shower width, the hadronic to electromagnetic energy ratio in the HCAL and ECAL, and isolations. Photon candidates that share the same energy cluster as an identified electron are vetoed. Due to algorithms designed to reject noise and out-of-time pileup, the default photon reconstruction vetoes high energy photons that are delayed by more than a few nanoseconds. This veto was not applied in the default photon reconstruction for previous data taking periods. A second set of out-of-time (OOT) photons is defined. Photons in this group are seeded by ECAL deposits whose signals are delayed by more than 3 ns. The OOT photon identification was separately optimized to discriminate displaced photons from backgrounds, and includes the use of the S_{major} and S_{minor} observables, which correspond to the major and

minor axes of the elliptical shower shape, defined as:

$$S_{\text{major}} = \frac{S_{\phi\phi} + S_{\eta\eta} + \sqrt{(S_{\phi\phi} - S_{\eta\eta})^2 + 4S_{\eta\phi}^2}}{2},$$
$$S_{\text{minor}} = \frac{S_{\phi\phi} + S_{\eta\eta} - \sqrt{(S_{\phi\phi} - S_{\eta\eta})^2 + 4S_{\eta\phi}^2}}{2} \quad (1)$$

where $S_{\phi\phi}$, $S_{\eta\eta}$, and $S_{\eta\phi}$ are the second moments of the spatial distribution of the energy deposits in the ECAL in $\eta - \phi$ coordinations. Since identification efficiencies are evaluated with $Z \to \ell\ell$ events, with the electrons reconstructed as photons, the sample is only partially representative of displaced electromagnetic objects. Any possible consequence of this approximation is included in the systematic uncertainty associated to the photon identification, described in Table 2.

Hadronic jets are reconstructed by clustering PF candidates using the infrared and collinear safe anti-k_T algorithm [40, 41]. Jets are clustered with distance parameter of 0.4. Further details of the performance of the jet reconstruction can be found in Ref. [42]. Jets used in any selection of this analysis are required to have $p_T > 30\,\text{GeV}$ and pseudorapidity $|\eta| < 3.0$.

The missing transverse momentum vector $\vec{p}_T^{\text{miss}}$ is computed as the negative vector sum of the transverse momenta of all the PF candidates in an event, and its magnitude is denoted as p_T^{miss} [43]. The $\vec{p}_T^{\text{miss}}$ is modified to account for corrections to the energy scale of the reconstructed jets in the event. Since OOT photons are not part of the standard reconstruction and are not considered in the list of PF candidates used to compute the $\vec{p}_T^{\text{miss}}$, a dedicated correction is applied to add back to the $\vec{p}_T^{\text{miss}}$ the energy of an OOT photon if it is selected as the leading photon of the event. Anomalous high-p_T^{miss} events can arise due to a variety of reconstruction failures, detector malfunctions or non-collisional backgrounds. Filters for vetoing such anomalous events are applied [44].

4.3 Photon time reconstruction

The time of arrival for a photon at the ECAL, t_{ECAL}, is calculated based on a weighted sum of the timestamps reconstructed from the signal pulse in each ECAL crystal comprising the photon cluster:

$$t_{\text{ECAL}} = \sum_i \frac{t_{\text{ECAL}}^i}{\sigma_i^2} \Big/ \sum_i \frac{1}{\sigma_i^2}, \quad (2)$$

where t_{ECAL}^i is the timestamp of the signal pulse in crystal i, and σ_i is the estimated time resolution of the signal pulse in crystal i [45]. The time resolution weights σ_i^2 are estimated based on the intrinsic time resolution of the ECAL crystal sensors, and scaled by the amplitude or energy contained in each crystal sensor:

$$\sigma_i^2 = \left(\frac{N}{A_i/\sigma_{N_i}}\right)^2 + 2C^2, \quad (3)$$

where A_i is the amplitude of the signal detected by crystal i, σ_{N_i} is the pedestal noise for crystal i, and N and C are constants fitted from a dedicated measurement of the time resolution of the crystal sensors.

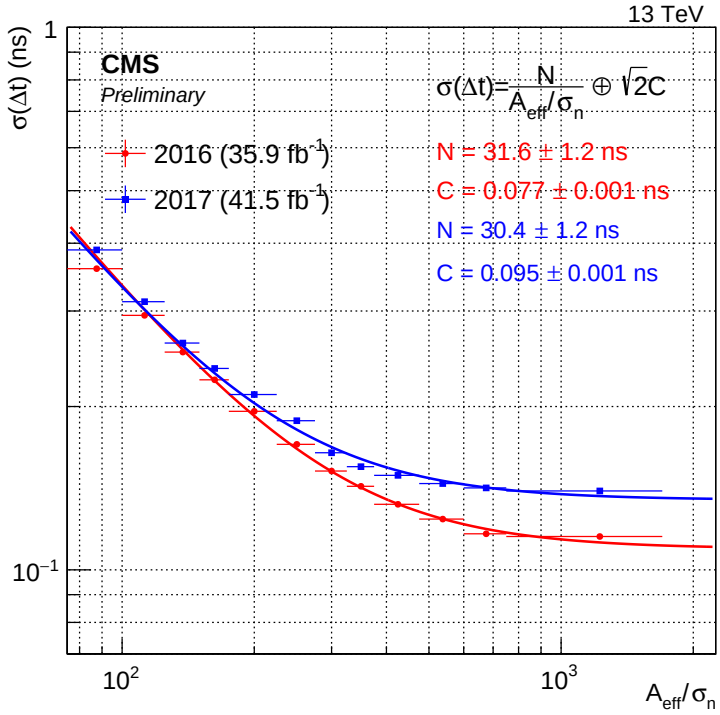

Figure 2: The time resolution between two neighboring ECAL crystals as a function of the effective amplitudes of the signals in the two crystals is shown for the 2016 and 2017 data sets.

To measure the crystal sensor time resolution, we follow the same procedure as done in Refs. [45] and [46]. Pairs of crystals from the same photon cluster are selected by requiring their energies are within 20% of each other and are nearest neighbors either in the η or ϕ directions and share the same readout electronics. The distributions of time differences measured in such crystal pairs are fitted to Gaussian functions in bins of the effective amplitude $A_{\text{eff}}/\sigma_{\text{N}}$, and the σ parameter of each fitted Gaussian function is plotted as a function of $A_{\text{eff}}/\sigma_{\text{N}}$. The effective amplitude is a combined amplitude of the signals in the two crystals and is defined as:

$$A_{\text{eff}}/\sigma_{\text{N}} = \frac{(A_1/\sigma_{\text{N}_1})(A_2/\sigma_{\text{N}_2})}{\sqrt{(A_1/\sigma_{\text{N}_1})^2 + (A_2/\sigma_{\text{N}_2})^2}} \tag{4}$$

The results for the 2016 and 2017 data sets are shown in Figure 2. These resolution measurements are fitted to the function form given in Equation 3, and the N and C parameters are extracted. These parameters are then used to calculate the weights for the photon timestamp in Equation 2. The observed worsening of the time resolution in 2017 is due to a loss of transparency of the crystals during the years and to the different levels of pileup in the two data taking periods.

To calibrate the photon timestamp response, electrons from $\text{Z} \to \ell\ell$ decays having a final state mass between between 60 and 150 GeV are reconstructed as photons. For each such photon candidate, the t_{ECAL} is subtracted by the time-of-flight from the primary vertex of the event to the impact location of the photon on the front face of the ECAL. The timestamps for each photon is recorded and the mean and σ parameters of the resulting distribution are extracted as a function of the energy of the photon object. The mean of the time response is corrected to zero for data and simulation, and the timestamps in the simulation events are smeared by an

additional gaussian random variable such that the resolution in simulation matches the measured resolution in data. The calibrated photon arrival time is defined as t_γ. These calibrations are applied also to the signal simulation samples in order to accurately predict the signal response, and their uncertainties are propagated to the shape prediction of the t_γ distribution for the signal as a systematic uncertainty. The time resolution of a single object is roughly 400 ps.

4.4 Event selection

Events with at least one photon in the barrel region of the detector ($|\eta| < 1.4442$) with p_T larger than 70 GeV are selected. This photon is required to pass the "tight" working point of the photon identification criteria whether it is a standard [39] or an OOT photon, with an average efficiency of about 70%, and a displaced photon identification requirement based on the S_major and S_minor variables. Electrons not matched to conversions are vetoed according to the procedure detailed in Ref. [39] for the 2016 data set; and for the 2017 data set, photons matched geometrically to charged particle tracks are vetoed in order to remain consistent with the selection of the high-level trigger. For the 2016 data set, a second photon with p_T larger than 40 GeV is required, with ($|\eta| < 2.5$) but excluding photons falling in the transition region between the barrel and endcap of the ECAL ($1.4442 < |\eta| < 1.566$). The requirement for the second photon is made in order to match the analogous requirement in the high-level trigger used for the 2016 data set. In order to maximize the sensitivity of the search, the 2017 data set is split into two event selection categories: the first with an explicit veto on a second photon, and a second category explicitly requiring a second photon satisfying the 2016 second photon criteria, referred to as the 2017γ and 2017$\gamma\gamma$ categories, respectively, for the remainder of this note. The second photon requirement helps to reduce background by one to two orders of magnitude, while the signal yield remains high for low to moderate lifetimes. Finally, three or more jets with p_T larger than 30 GeV are required, and for the 2017 data set only, the H_T is required to be larger than 400 GeV to obtain high efficiency with respect to the analogous trigger requirement.

For the 2016 data set and 2017$\gamma\gamma$ data set, for a given neutralino proper decay length, the signal yield increases as a function of the SUSY breaking scale Λ by roughly a factor of two over the range of points considered for this analysis — i.e. Λ from 100 TeV to 400 TeV. The signal efficiency times acceptance for the lowest Λ is roughly $10.0 \pm 0.1\%$ and $0.15 \pm 0.01\%$ for neutralino proper decay lengths of 10 and 10000 cm, respectively. For the 2017γ data set, the signal efficiency times acceptance varies from $5.5 \pm 0.1\%$ to $10.4 \pm 0.2\%$ for a neutralino proper decay length of 10 cm, and from $0.22 \pm 0.03\%$ to $0.65 \pm 0.05\%$ for a neutralino proper decay length of 10000 cm. These values can be understood as the increase in Λ results in harder photon spectra and an increase in jet activity, while an increase in the neutralino proper decay length results in either one or both of the NLSPs decaying outside the fiducial region of the ECAL.

Figure 3 shows the distributions of the number of events as a function of $p_\mathrm{T}^\mathrm{miss}$, for low and high t_γ; and t_γ, for low and high $p_\mathrm{T}^\mathrm{miss}$, in data for the 2016, 2017γ, and 2017$\gamma\gamma$ event selections. In addition, the distribution of events with a representative signal point (i.e. GMSB: $\Lambda = 200$ TeV, $c\tau = 200$ cm) is also shown, scaled by the production cross section times the integrated luminosity in the regions where this signal is most sensitive: large $p_\mathrm{T}^\mathrm{miss}$ and t_γ.

5 Signal extraction and background estimation

The $p_{\mathrm{T}}^{\mathrm{miss}}$ and t_γ are used as the discriminating observables to distinguish signal from background. Four regions are defined based on the values of the $p_{\mathrm{T}}^{\mathrm{miss}}$ and t_γ observables. Region A has low $p_{\mathrm{T}}^{\mathrm{miss}}$ and low t_γ; region B has high $p_{\mathrm{T}}^{\mathrm{miss}}$ and low t_γ; region C has high $p_{\mathrm{T}}^{\mathrm{miss}}$ and high t_γ; and region D has low $p_{\mathrm{T}}^{\mathrm{miss}}$ and high t_γ. Signals with large lifetimes are concentrated in region C with large $p_{\mathrm{T}}^{\mathrm{miss}}$ and large t_γ, while signals with shorter lifetimes will tend to occupy region B with large $p_{\mathrm{T}}^{\mathrm{miss}}$ and low t_γ. In contrast, backgrounds are concentrated in region A with low $p_{\mathrm{T}}^{\mathrm{miss}}$ and low t_γ. In general, region C is the most sensitive region with largest signal to background ratio. After the offline selection is applied, the main background contribution is from collisional processes with high $p_{\mathrm{T}}^{\mathrm{miss}}$, which have the same timing distribution as collisional events with low $p_{\mathrm{T}}^{\mathrm{miss}}$, ensuring that the two discriminating variables are uncorrelated for background processes. This includes proton collisions from satellite bunches, i.e. proton bunches in adjacent RF "buckets", which are spaced ~ 2.5 ns between the main bunches. The non-collisional backgrounds, which include cosmic ray muons, beam halo muons, and electronic noise deposits, are rejected to a negligible level by the number of jets requirement and the photon selections.

As the $p_{\mathrm{T}}^{\mathrm{miss}}$ and t_γ observables are uncorrelated, it is assumed that the background distribution can be factorized into the product of the distributions of these two observables. With this assumption, the background yield in the signal-enriched region C can be estimated based on the relationship: $\mathrm{N_C} = (\mathrm{N_D}\mathrm{N_B})/\mathrm{N_A}$, where $\mathrm{N_X}$ is the number of background events in region X. This method of background estimation is defined as the "ABCD" method. In order to account for nonnegligible signal contamination in regions A, B, and D a modified ABCD method is used where a simultaneous fit is performed with the signal strength included as a floating parameter that scales the signal yield uniformly in each region. The background component of the fit is constrained to obey the standard ABCD relationship, within the bounds of a small systematic uncertainty derived from a validation check of the method in a control region.

For each point in the signal model parameter space (Λ and $c\tau$), the boundaries in $p_{\mathrm{T}}^{\mathrm{miss}}$ and t_γ that define the A, B, C, and D bins are chosen to yield optimal expected sensitivity. In order to remain unbiased during the optimization procedure, estimates of the background yields are provided using the observed yield in data for bin A while the background yields in the remaining bins are taken from the ratios of integrals of one-dimensional shape templates of $p_{\mathrm{T}}^{\mathrm{miss}}$ and t_γ for the bin splits being considered between bins A, B and A, D, respectively. These template shapes are derived from the data in regions with negligible signal yield. The resulting optimized bin boundaries in t_γ and $p_{\mathrm{T}}^{\mathrm{miss}}$ are summarized in Table 1 for all the SPS8 model parameter space points considered. To simplify the analysis, groups of similar signal model parameters share the same optimized bin boundaries.

Table 1: The optimized bin boundaries for the t_γ (first number in units of ns) and $p_{\mathrm{T}}^{\mathrm{miss}}$ (second number in units of GeV) are shown for different GMSB SPS8 signal model parameter space points considered in the search for each data set category.

$c\tau$ (cm)	$\Lambda \leq 300$ TeV			$\Lambda > 300$ TeV		
	2016	2017γ	2017$\gamma\gamma$	2016	2017γ	2017$\gamma\gamma$
(0,10]	0, 250	0.5, 300	0.5, 150	0, 250	0.5, 300	0.5, 200
(10, 10000]	1.5, 100	1.5, 200	1.5, 150	1.5, 150	1.5, 300	1.5, 200

To validate that the $p_{\mathrm{T}}^{\mathrm{miss}}$ and t_γ observables are uncorrelated, we define control regions (CR) that isolate different SM processes similar to the backgrounds that are expected in our signal

region. The γ + jets CR, dominated by the γ + jets process, is defined as events satisfying the same requirements as the signal region, but having fewer than three jets. The multijet CR, dominated by QCD multijet production, is defined as events satisfying the same requirements as the signal region, but inverting the isolation requirement on the leading photon. The correlation coefficients between $p_{\mathrm{T}}^{\mathrm{miss}}$ and t_γ are measured to be less than 1% for both γ + jets CR and multijet CR in both data sets and determine that they are negligible.

6 Uncertainties

The dominant uncertainty for this search is the statistical uncertainty on the ratio parameters for the background prediction from the fit.

There are several systematic uncertainties that affect the prediction of the signal yield in all four bins. They primarily result from uncertainties in the simulation and modeling of the signal efficiency for various selection requirements that are made. These systematic uncertainties include the uncertainty in the integrated luminosity measurement [47]-[48], the simulated energy scale and resolution of the photons and jets, and trigger and photon identification efficiencies. For all these cases, dedicated measurements are performed that evaluate corrections and uncertainties in efficiencies and energy scales in the simulated signal events, and these uncertainties are propagated to our signal yield predictions as an uncertainty on the predicted shape of the discriminating observables $p_{\mathrm{T}}^{\mathrm{miss}}$ and t_γ. The calibration of the timestamp discussed in Section 4.3 contains uncertainties that affect both the offset and resolution of t_γ, and are propagated on the shape prediction for the t_γ distribution for the signal points.

As the background estimation is only constrained by requiring that discriminating observables $p_{\mathrm{T}}^{\mathrm{miss}}$ and t_γ are uncorrelated, any residual correlation is treated as an uncertainty in the background prediction. This is estimated by measuring the difference in observed yields in the γ + jets and multijet CRs from the predicted background in bin C using t_γ and $p_{\mathrm{T}}^{\mathrm{miss}}$ bin splittings similar to the signal regions. Since the longer lifetime signal models use a much higher t_γ split, the observed and predicted yields in bin C are significantly lower than the shorter lifetime models, resulting in a larger uncertainty on the closure of the background prediction. Table 2 provides a summary of the systematic uncertainties in this analysis and their assigned values to each data set, as well as additional information about how the uncertainties are correlated.

7 Results and interpretation

Table 3 lists the observed yields, post-fit background predicted yields for the background-only fit in each of the four bins for all the t_γ-$p_{\mathrm{T}}^{\mathrm{miss}}$ selections used. No statistically significant deviation from the background expectation is observed. The search result is thus interpreted in terms of limits on the neutralino production cross section for scenarios in the GMSB SPS8 signal model set.

The modified frequentist criterion $\mathrm{CL_s}$ [49–51] with the profile likelihood ratio test statistic is used to evaluate the 95% confidence level (CL) observed and expected limits on the signal production cross sections. The limits are shown as a function of the mass of the neutralino NLSP $\tilde{\chi}_1^0$ (linearly related to the SUSY breaking scale, Λ) and the proper decay length of the neutralino in Figure 4. The two photon category (2016 and 2017$\gamma\gamma$) and the one photon category (2017γ) are complementary as the sensitivity at small proper decay length is better for the 2016 and 2017$\gamma\gamma$ categories due to the extra background suppression from requiring two photons,

Table 2: Summary table of systematics and their assigned values in this analysis. Also included are notes on whether each source affects signal yields (Sig) or background (Bkg) estimates, to which bins each uncertainty applies, and how the correlations of the uncertainties between the different data sets are treated. We assign different values for the uncertainty on the closure of the background prediction for short and long lifetime signal models.

Systematic uncertainty	Sig/Bkg	Bins	2016	2017	Correlation
Integrated luminosity	Sig	A,B,C,D	2.5%	2.3%	Uncorrelated
Photon energy scale	Sig	A,B,C,D	1%	2%	100% Correlated
Photon energy resolution	Sig	A,B,C,D	1%	1%	100% Correlated
Jet energy scale	Sig	A,B,C,D	1.5%	2%	100% Correlated
Jet energy resolution	Sig	A,B,C,D	1.5%	1.5%	Uncorrelated
Photon time bias	Sig	A,B,C,D	1.5%	1%	100% Correlated
Photon time resolution	Sig	A,B,C,D	0.5%	0.5%	100% Correlated
Trigger efficiency	Sig	A,B,C,D	2%	$<$1%	Uncorrelated
Photon identification	Sig	A,B,C,D	2%	3%	100% Correlated
Closure in bin C ($c\tau \leq 10$ cm)	Bkg	C	2%	3.5%	100% Correlated
Closure in bin C ($c\tau > 10$ cm)	Bkg	C	90%	90%	100% Correlated

while the sensitivity at large proper decay lengths is better for the 2017γ analysis because of significantly improved signal acceptance from the dedicated displaced single photon trigger. As a result, the sensitivity to signal models with proper lifetimes greater than the ECAL timing resolution for a single object is improved compared to previous results. For neutralino proper decay lengths $c\tau$ of 10^1, 10^2, 10^3, and 10^4 cm, masses up to about 320, 525, 360, and 215 GeV are excluded at 95% CL, respectively.

8 Summary

A search for long-lived particles (LLP) decaying to a photon and a weakly-interacting particle using proton-proton collisions at a center of mass energy of 13 TeV collected by the CMS experiment is presented. Such photons impact the electromagnetic calorimeter at a nonnormal impact angles and at delayed times, and this striking combination of features is exploited to suppress backgrounds. The search is performed using a combination of the 2016 and 2017 data sets, corresponding to a total integrated luminosity of 77.4 fb^{-1}. A combination of single photon and diphoton events is used for the search, which yields complementary sensitivity at larger and smaller LLP proper decay lengths, respectively. The results are interpreted in the context of supersymmetry with gauge-mediated SUSY breaking using the SPS8 benchmark model. For neutralino proper decay lengths of 10^1, 10^2, 10^3, and 10^4 cm, masses up to about 320, 525, 360, and 215 GeV are excluded at 95% CL, respectively. The previous best limits are extended by about one order of magnitude in the neutralino proper decay length, and the mass reach is improved by about 100 GeV.

Table 3: Observed events ($N_{\text{obs}}^{\text{data}}$) and predicted background post-fit yields from background-only fit ($N_{\text{bkg}}^{\text{post-fit}}$) in bins A, B, C and D for data from different years and categories and for different t_γ and $p_{\text{T}}^{\text{miss}}$ split options. In addition, the predicted post-fit yields from the background-only fit masking bin C ($N_{\text{bkg(mask)}}^{\text{post-fit}}$) are provided as a test of closure. Uncertainties for $N_{\text{bkg}}^{\text{post-fit}}$ and $N_{\text{bkg(mask)}}^{\text{post-fit}}$ are the sum in quadrature of the statistical and systematic uncertainties (statistical uncertainties dominate).

Year / Category	Bin Split [t_γ (ns), $p_{\text{T}}^{\text{miss}}$ (GeV)]		A	B	C	D
2016$\gamma\gamma$	(0, 250)	$N_{\text{obs}}^{\text{data}}$	16139	41	62	18826
		$N_{\text{bkg}}^{\text{post-fit}}$	16133 ± 114	47.5 ± 4.8	55.6 ± 5.6	18832 ± 130
		$N_{\text{bkg(mask)}}^{\text{post-fit}}$	16139 ± 114	41.0 ± 6.5	47.8 ± 7.7	18826 ± 130
	(1.5, 100)	$N_{\text{obs}}^{\text{data}}$	33760	1302	1	5
		$N_{\text{bkg}}^{\text{post-fit}}$	33759 ± 164	1303 ± 37	0.29 ± 0.28	5.7 ± 2.2
		$N_{\text{bkg(mask)}}^{\text{post-fit}}$	33761 ± 165	1302 ± 37	0.19 ± 0.21	5.0 ± 2.1
	(1.5, 150)	$N_{\text{obs}}^{\text{data}}$	34595	467	0	6
		$N_{\text{bkg}}^{\text{post-fit}}$	34596 ± 166	467 ± 22	0.08 ± 0.08	5.9 ± 2.3
		$N_{\text{bkg(mask)}}^{\text{post-fit}}$	34596 ± 167	467 ± 22	0.08 ± 0.09	6.0 ± 2.3
2017γ	(0.5, 300)	$N_{\text{obs}}^{\text{data}}$	458372	281	41	67655
		$N_{\text{bkg}}^{\text{post-fit}}$	458368 ± 660	281 ± 15	41.4 ± 2.4	67656 ± 280
		$N_{\text{bkg(mask)}}^{\text{post-fit}}$	458369 ± 662	281 ± 16	41.5 ± 2.7	67657 ± 281
	(1.5, 200)	$N_{\text{obs}}^{\text{data}}$	524652	1364	1	332
		$N_{\text{bkg}}^{\text{post-fit}}$	524653 ± 706	1364 ± 36	0.9 ± 0.8	332 ± 20
		$N_{\text{bkg(mask)}}^{\text{post-fit}}$	524653 ± 704	1364 ± 35	0.9 ± 1.0	332 ± 20
	(1.5, 300)	$N_{\text{obs}}^{\text{data}}$	525694	322	0	333
		$N_{\text{bkg}}^{\text{post-fit}}$	525694 ± 707	322 ± 17	0.19 ± 0.21	333 ± 20
		$N_{\text{bkg(mask)}}^{\text{post-fit}}$	525694 ± 704	322 ± 17	0.20 ± 0.24	333 ± 20
2017$\gamma\gamma$	(0.5, 150)	$N_{\text{obs}}^{\text{data}}$	21640	362	56	3201
		$N_{\text{bkg}}^{\text{post-fit}}$	21638 ± 143	364 ± 17	54.0 ± 3.0	3203 ± 61
		$N_{\text{bkg(mask)}}^{\text{post-fit}}$	21639 ± 143	362 ± 18	53.6 ± 3.3	3201 ± 61
	(0.5, 200)	$N_{\text{obs}}^{\text{data}}$	21863	139	24	3233
		$N_{\text{bkg}}^{\text{post-fit}}$	21860 ± 144	142 ± 11	21.1 ± 1.7	3236 ± 61
		$N_{\text{bkg(mask)}}^{\text{post-fit}}$	21863 ± 144	139 ± 11	20.6 ± 1.8	3233 ± 61
	(1.5, 150)	$N_{\text{obs}}^{\text{data}}$	24824	418	0	17
		$N_{\text{bkg}}^{\text{post-fit}}$	24824 ± 154	418 ± 20	0.25 ± 0.28	16.7 ± 4.4
		$N_{\text{bkg(mask)}}^{\text{post-fit}}$	24824 ± 154	418 ± 20	0.29 ± 0.36	17.0 ± 4.4
	(1.5, 200)	$N_{\text{obs}}^{\text{data}}$	25079	163	0	17
		$N_{\text{bkg}}^{\text{post-fit}}$	25079 ± 154	163 ± 12	0.11 ± 0.12	16.9 ± 4.4
		$N_{\text{bkg(mask)}}^{\text{post-fit}}$	25079 ± 154	163 ± 12	0.11 ± 0.14	17.0 ± 4.4

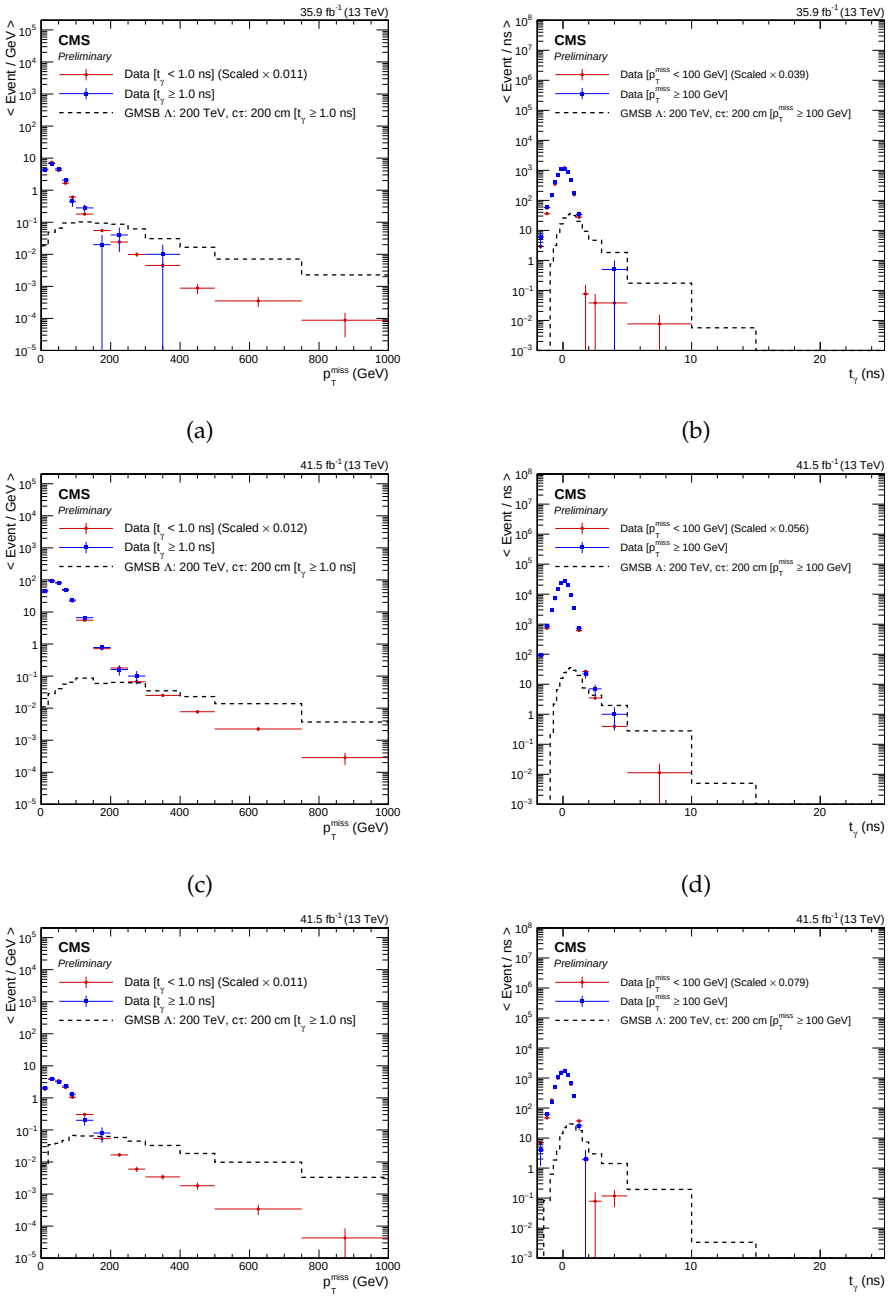

Figure 3: Distributions of the number events in data and a representative signal point (GMSB: $\Lambda = 200\,\text{TeV}, c\tau = 200\,\text{cm}$) scaled by the production cross section times the integrated luminosity as functions of $p_{\text{T}}^{\text{miss}}$ (a, c, e) and t_γ(b, d, f) using the 2016 (a, b), 2017γ (c, d) and 2017$\gamma\gamma$ (e, f) event selections. The $p_{\text{T}}^{\text{miss}}$ distribution in data is split for events with $t_\gamma < 1\,\text{ns}$ (red, scaled down to match the total number of events with $t_\gamma \geq 1\,\text{ns}$) and $t_\gamma \geq 1\,\text{ns}$ (blue), while the signal (black) is shown for late times. The t_γ distribution in data is split for events with $p_{\text{T}}^{\text{miss}} < 100\,\text{GeV}$ (red, scaled down to match the total number of events with $p_{\text{T}}^{\text{miss}} \geq 100\,\text{GeV}$) and $p_{\text{T}}^{\text{miss}} \geq 100\,\text{GeV}$ (blue), while the signal (black) is shown for high $p_{\text{T}}^{\text{miss}}$. The entries in each bin are normalized by the bin width, where the horizontal bars on data indicate the bin boundaries. The last bin in each plot contains overflow events.

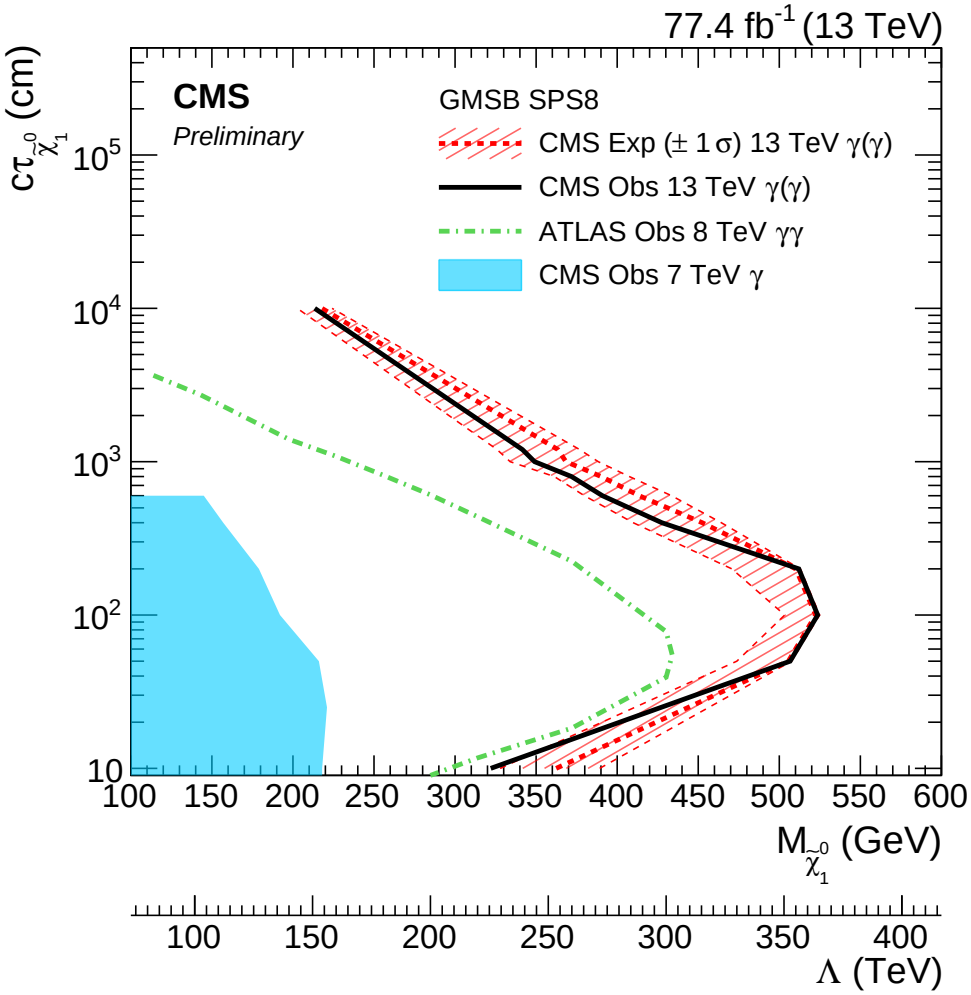

Figure 4: The observed 95% CL exclusion contours on the signal production cross section are shown as a function of the neutralino proper decay length $c\tau_{\tilde{\chi}_1^0}$ versus the neutralino mass in the GMSB SPS8 model.

References

[1] P. Ramond, "Dual theory for free fermions", *Phys. Rev. D* **3** (1971) 2415, doi:10.1103/PhysRevD.3.2415.

[2] P. Ramond, "An interpretation of dual theories", *Nuovo Cim. A* **4** (1971) 544, doi:10.1007/BF02731370.

[3] Yu. A. Golfand and E. P. Likhtman, "Extension of the algebra of Poincaré group generators and violation of P invariance", *JETP Lett.* **13** (1971) 323.

[4] D. V. Volkov and V. P. Akulov, "Possible universal neutrino interaction", *JETP Lett.* **16** (1972) 438, doi:10.1007/BFb0105270.

[5] J. Wess and B. Zumino, "Supergauge transformations in four-dimensions", *Nucl. Phys. B* **70** (1974) 39, doi:10.1016/0550-3213(74)90355-1.

[6] D. Z. Freedman, P. van Nieuwenhuizen, and S. Ferrara, "Progress toward a theory of supergravity", *Phys. Rev. D* **13** (1976) 3214, doi:10.1103/PhysRevD.13.3214.

[7] S. Deser and B. Zumino, "Consistent supergravity", *Phys. Lett. B* **62** (1976) 335, doi:10.1016/0370-2693(76)90089-7.

[8] D. Z. Freedman and P. van Nieuwenhuizen, "Properties of supergravity theory", *Phys. Rev. D* **14** (1976) 912, doi:10.1103/PhysRevD.14.912.

[9] S. Ferrara and P. van Nieuwenhuizen, "Consistent supergravity with complex spin 3/2 gauge fields", *Phys. Rev. Lett.* **37** (1976) 1669, doi:10.1103/PhysRevLett.37.1669.

[10] P. Fayet, "Supergauge invariant extension of the Higgs mechanism and a model for the electron and its neutrino", *Nucl. Phys. B* **90** (1975) 104, doi:10.1016/0550-3213(75)90636-7.

[11] A. H. Chamseddine, R. L. Arnowitt, and P. Nath, "Locally supersymmetric grand unification", *Phys. Rev. Lett.* **49** (1982) 970, doi:10.1103/PhysRevLett.49.970.

[12] R. Barbieri, S. Ferrara, and C. A. Savoy, "Gauge models with spontaneously broken local supersymmetry", *Phys. Lett. B* **119** (1982) 343, doi:10.1016/0370-2693(82)90685-2.

[13] L. J. Hall, J. D. Lykken, and S. Weinberg, "Supergravity as the messenger of supersymmetry breaking", *Phys. Rev. D* **27** (1983) 2359, doi:10.1103/PhysRevD.27.2359.

[14] G. L. Kane, C. F. Kolda, L. Roszkowski, and J. D. Wells, "Study of constrained minimal supersymmetry", *Phys. Rev. D* **49** (1994) 6173, doi:10.1103/PhysRevD.49.6173, arXiv:hep-ph/9312272.

[15] G. F. Giudice and R. Rattazzi, "Theories with gauge mediated supersymmetry breaking", *Phys. Rept.* **322** (1999) 419, doi:10.1016/S0370-1573(99)00042-3, arXiv:hep-ph/9801271.

[16] S. Dimopoulos, M. Dine, S. Raby, and S. D. Thomas, "Experimental signatures of low-energy gauge mediated supersymmetry breaking", *Phys. Rev. Lett.* **76** (1996) 3494, doi:10.1103/PhysRevLett.76.3494, arXiv:hep-ph/9601367.

[17] P. Fayet, "Mixing between gravitational and weak interactions through the massive gravitino", *Phys. Lett. B* **70** (1977) 461, doi:10.1016/0370-2693(77)90414-2.

[18] H. Baer, M. Brhlik, C. H. Chen, and X. Tata, "Signals for the minimal gauge-mediated supersymmetry breaking model at the Fermilab Tevatron collider", *Phys. Rev. D* **55** (1997) 4463, doi:10.1103/PhysRevD.55.4463, arXiv:hep-ph/9610358.

[19] H. Baer, P. G. Mercadante, X. Tata, and Y. L. Wang, "Reach of Tevatron upgrades in gauge-mediated supersymmetry breaking models", *Phys. Rev. D* **60** (1999) 055001, doi:10.1103/PhysRevD.60.055001, arXiv:hep-ph/9903333.

[20] S. Dimopoulos, S. Thomas, and J. D. Wells, "Sparticle spectroscopy and electroweak symmetry breaking with gauge-mediated supersymmetry breaking", *Nucl. Phys. B* **488** (1997) 39, doi:10.1016/S0550-3213(97)00030-8, arXiv:hep-ph/9609434.

[21] J. R. Ellis, J. L. Lopez, and D. V. Nanopoulos, "Analysis of LEP constraints on supersymmetric models with a light gravitino", *Phys. Lett. B* **394** (1997) 354, doi:10.1016/S0370-2693(97)00019-1, arXiv:hep-ph/9610470.

[22] M. Dine, A. E. Nelson, Y. Nir, and Y. Shirman, "New tools for low energy dynamical supersymmetry breaking", *Phys. Rev. D* **53** (1996) 2658, doi:10.1103/PhysRevD.53.2658, arXiv:hep-ph/9507378.

[23] G. F. Giudice and R. Rattazzi, "Gauge-mediated supersymmetry breaking", in *Perspectives on supersymmetry*, p. 355. World Scientific, Singapore, 1998.

[24] B. C. Allanach et al., "The Snowmass points and slopes: Benchmarks for SUSY searches", *Eur. Phys. J. C* **25** (2002) 113, doi:10.1007/s10052-002-0949-3, arXiv:hep-ph/0202233.

[25] C. H. Chen and J. F. Gunion, "Maximizing hadron collider sensitivity to gauge mediated supersymmetry breaking models", *Phys. Lett. B* **420** (1998) 77, doi:10.1016/S0370-2693(97)01428-7, arXiv:hep-ph/9707302.

[26] CMS Collaboration, "Search for long-lived particles decaying to photons and missing energy in proton-proton collisions at $\sqrt{s} = 7$ TeV", *Phys. Lett. B* **722** (2013) 273, doi:10.1016/j.physletb.2013.04.027, arXiv:1212.1838.

[27] ATLAS Collaboration, "Search for nonpointing and delayed photons in the diphoton and missing transverse momentum final state in 8 TeV pp collisions at the LHC using the ATLAS detector", *Phys. Rev. D* **90** (2014) 112005, doi:10.1103/PhysRevD.90.112005, arXiv:1409.5542.

[28] CMS Collaboration, "The CMS experiment at the CERN LHC", *JINST* **3** (2008) S08004, doi:10.1088/1748-0221/3/08/S08004.

[29] CMS Collaboration, "The CMS trigger system", *JINST* **12** (2017) P01020, doi:10.1088/1748-0221/12/01/P01020, arXiv:1609.02366.

[30] J. Alwall et al., "Comparative study of various algorithms for the merging of parton showers and matrix elements in hadronic collisions", *Eur. Phys. J. C* **53** (2008) 473, doi:10.1140/epjc/s10052-007-0490-5, arXiv:0706.2569.

[31] T. Gleisberg et al., "Event generation with SHERPA 1.1", *JHEP* **02** (2009) 007, doi:10.1088/1126-6708/2009/02/007, arXiv:0811.4622.

[32] T. Sjöstrand, S. Mrenna, and P. Skands, "A brief introduction to PYTHIA 8.1", *Comp. Phys. Commun.* **178** (2008) 852, doi:10.1016/j.cpc.2008.01.036.

[33] P. Skands, S. Carrazza, and J. Rojo, "Tuning PYTHIA 8.1: the Monash 2013 tune", *Eur. Phys. J. C* **74** (2014) 3024, doi:10.1140/epjc/s10052-014-3024-y.

[34] CMS Collaboration, "Extraction and validation of a new set of CMS PYTHIA8 tunes from underlying-event measurements", Technical Report CMS-PAS-GEN-17-001, CERN, Geneva, 2018.

[35] NNPDF Collaboration, "Parton distributions for the LHC Run II", *JHEP* **04** (2015) 040, doi:10.1007/JHEP04(2015)040, arXiv:1410.8849.

[36] NNPDF Collaboration, "Parton distributions from high-precision collider data", *Eur. Phys. J. C* **77** (2017) 663, doi:10.1140/epjc/s10052-017-5199-5, arXiv:1706.00428.

[37] GEANT4 Collaboration, "GEANT4—a simulation toolkit", *Nucl. Instrum. Meth. A* **506** (2003) 250, doi:10.1016/S0168-9002(03)01368-8.

[38] CMS Collaboration, "Particle-flow reconstruction and global event description with the CMS detector", *JINST* **12** (2017) P10003, doi:10.1088/1748-0221/12/10/P10003, arXiv:1706.04965.

[39] CMS Collaboration, "Performance of photon reconstruction and identification with the CMS detector in proton-proton collisions at $\sqrt{s} = 8$ TeV", *JINST* **10** (2015) P08010, doi:10.1088/1748-0221/10/08/P08010, arXiv:1502.02702.

[40] M. Cacciari, G. P. Salam, and G. Soyez, "The anti-k_{T} jet clustering algorithm", *JHEP* **04** (2008) 063, doi:10.1088/1126-6708/2008/04/063, arXiv:0802.1189.

[41] M. Cacciari, G. P. Salam, and G. Soyez, "FastJet user manual", *Eur. Phys. J. C* **72** (2012) 1896, doi:10.1140/epjc/s10052-012-1896-2, arXiv:1111.6097.

[42] CMS Collaboration, "Jet algorithms performance in 13 TeV data", CMS Physics Analysis Summary CMS-PAS-JME-16-003, CERN, 2017.

[43] CMS Collaboration, "Performance of missing transverse momentum in pp collisions at $\sqrt{s} = 13$ TeV using the CMS detector", CMS Physics Analysis Summary CMS-PAS-JME-17-001, CERN, 2018.

[44] CMS Collaboration, "Performance of missing transverse momentum reconstruction in proton-proton collisions at $\sqrt{s}$ = 13 TeV using the CMS detector", *JINST* **14** (2019), no. 07, P07004, doi:10.1088/1748-0221/14/07/p07004, arXiv:1903.06078.

[45] CMS Collaboration, "Time Reconstruction and Performance of the CMS Electromagnetic Calorimeter", *JINST* **5** (2010) T03011, doi:10.1088/1748-0221/5/03/T03011, arXiv:0911.4044.

[46] D. del Re, "Timing performance of the CMS ECAL and prospects for the future", *J. Phys. Conf. Ser.* **587** (2015), no. 1, 012003, doi:10.1088/1742-6596/587/1/012003.

[47] CMS Collaboration, "CMS Luminosity Measurements for the 2016 Data Taking Period", Technical Report CMS-PAS-LUM-17-001, CERN, Geneva, 2017.

[48] CMS Collaboration, "CMS luminosity measurement for the 2017 data-taking period at $\sqrt{s} = 13$ TeV", Technical Report CMS-PAS-LUM-17-004, CERN, Geneva, 2018.

[49] A. L. Read, "Presentation of search results: The CL_s technique", *J. Phys. G* **28** (2002) 2693, doi:10.1088/0954-3899/28/10/313.

[50] T. Junk, "Confidence level computation for combining searches with small statistics", *Nucl. Instrum. Meth. A* **434** (1999) 435, doi:10.1016/S0168-9002(99)00498-2, arXiv:hep-ex/9902006.

[51] ATLAS and CMS Collaborations, "Procedure for the LHC Higgs boson search combination in summer 2011", CMS NOTE/ATL-PHYS-PUB ATL-PHYS-PUB-2011-011, CMS-NOTE-2011-005, CERN, 2011.